



Regular article

Co content effect on elastic strain limit in ZrCuNiAlCo bulk metallic glasses

Y. Dong^a, R. Wunderlich^a, J. Biskupek^b, Q.P. Cao^c, X.D. Wang^c, D.X. Zhang^d, J.Z. Jiang^{c,*}, H.-J. Fecht^{a,*}^a Institute of Micro and Nanomaterials, University of Ulm, Albert-Einstein Allee 47, 89081 Ulm, Germany^b Electron Microscopy Group of Materials Science, University of Ulm, Albert-Einstein Allee 11, 89081 Ulm, Germany^c International Center for New-Structured Materials, State Key Laboratory of Silicon Materials and School of Materials Science and Engineering, Zhejiang University, Hangzhou 310027, People's Republic of China^d State Key Laboratory of Modern Optical Instrumentation, Zhejiang University, Hangzhou 310027, People's Republic of China

ARTICLE INFO

Article history:

Received 13 April 2017

Received in revised form 5 May 2017

Accepted 5 May 2017

Available online 18 May 2017

Keywords:

Bulk metallic glass

Inhomogeneous structure

Elastic strain limit

Mechanical properties

ABSTRACT

The microstructures and mechanical properties of $\text{Zr}_{64-x}\text{Ni}_{10}\text{Al}_7\text{Cu}_{19}\text{Co}_x$ ($x = 0-16$ at.%) bulk metallic glasses (BMGs) were investigated as a function of cobalt content. Due to negative mixing enthalpy between cobalt and zirconium, the atomic packing structure of studied BMGs changes with the addition of cobalt while the positive mixing enthalpy between cobalt and copper leads to phase separation and the formation of nanoglass with glassy grain sizes of about 5–10 nm. With the unique topological structure, the stored recoverable elastic energy in these studied BMGs increases dramatically with the increasing cobalt content. The $\text{Zr}_{55.7}\text{Ni}_{10}\text{Al}_7\text{Cu}_{19}\text{Co}_{8.3}$ BMG exhibits excellent mechanical properties at ambient temperature.

© 2017 Acta Materialia Inc. Published by Elsevier Ltd. All rights reserved.

Bulk metallic glasses (BMGs) are alloys without long-range lattice atomic packing, which are different from the normal crystalline metals. Because of their special structures, such as without dislocations, BMGs have some excellent properties including high strength, high hardness, and good corrosion resistance. Unlike the crystalline metals in which the plastic deformation is driven by the movement of the dislocation, the plastic deformation in BMGs is located in narrow regions named shear bands which are easy to propagate throughout the material leading to catastrophic failure. Due to their special deformation mechanism, high elastic strain limit is an important advantage for BMGs as structural materials which can reach 1.8% while it is only around 0.2% for normal crystalline alloys. Consequently, BMGs can store large elastic energy which makes them potential application as micromechanics, drivers, sports equipment [1–3]. Mechanical behaviors of BMGs have been considerably investigated [4,5]. It was reported that the higher the Poisson's ratio γ and the lower shear modulus/bulk modulus ratio, the better the plastic properties of the BMGs [6,7]. Mechanical properties of BMGs were also found to be linked with their glass transition temperature T_g [8,9]. Experiments revealed that the introduction of inhomogeneous structures can improve mechanical properties of BMGs [10–13]. For example, as a new kind of inhomogeneous material, nanoglass materials, which was conceived by Gleiter, consisting of nanometer-sized glassy regions connected by glass/glass interfaces [14], present excellent mechanical and other properties due to their unique microstructure [15–17].

In this work, our scenario is to add an element which has positive mixing enthalpy with another element in the studied BMGs to achieve inhomogeneous structure although this scheme may reduce the glass forming ability, however, can also improve mechanical properties of BMGs [18–20]. The ZrCuNiAl system is a well-studied BMG system [21–25], in which good glass forming ability and good plasticity were reported in some composition range. Thus, here we selected this alloy system by adding cobalt element because of the positive mixing enthalpy with copper (6 kJ/mol), and the negative mixing enthalpy with zirconium (−41 kJ/mol) [26,27]. Here, we report the results on the cobalt composition dependences of microstructures and mechanical properties in $\text{Zr}_{64-x}\text{Ni}_{10}\text{Al}_7\text{Cu}_{19}\text{Co}_x$ ($x = 0-16$ at.%) alloys. Various techniques, including X-ray diffraction (XRD) with Cu K_α radiation, pair-distribution function (PDF) obtained from synchrotron radiation source, extended X-ray absorption of fine structure analysis (EXAFS), differential scanning calorimeter (DSC), transmission electron microscopy (TEM) and scanning electron microscopy (SEM), were applied to characterize structures of studied samples. Uniaxial compression, nanoindentation, in situ compression in SEM and ultrasonic measurements were carried out to study the mechanical behaviors of all studied samples. It is found that the $\text{Zr}_{55.7}\text{Ni}_{10}\text{Al}_7\text{Cu}_{19}\text{Co}_{8.3}$ BMG developed here exhibits excellent mechanical properties at ambient temperature, i.e., about 2.8% elastic strain limit, about 2.3 GPa yielding strength, about 4% compression plastic strain, Young modulus of 84.4 GPa, Poisson ratio of 0.393 and the ratio of shear modulus to bulk modulus of 0.231.

$\text{Zr}_{64-x}\text{Ni}_{10}\text{Al}_7\text{Cu}_{19}\text{Co}_x$ ($x = 0-16$ at.%) ingots with different compositions were prepared with pure elements by arc melting in argon

* Corresponding authors.

E-mail address: jiangjz@zju.edu.cn (J.Z. Jiang).

atmosphere. All the ingots were remelted five times to get the homogeneous composition, which were then suction casted into water cooled copper mold. Two different sample shapes were casted, rods with 2 mm diameter and disks with 12 mm diameter and 1.8 mm thickness. The structures of all samples were studied using X-ray diffraction (XRD with Cu-K α radiation). The thermal properties of the BMGs were analyzed by continuous heating in a differential scan calorimeter under flowing high purity Ar with a heating rate of 20 K/min. Two identical DSC measurements were made on each sample. From the second run, the baseline was gotten with the sample in its crystalline state. The final curve can be obtained by subtraction of the baseline from the first DSC run. To characterize atomic structures, synchrotron radiation-based XRD measurements using a wavelength of 0.124 Å at HASYLAB/DESY in Hamburg were carried out for BMG samples. After background subtraction and corrections for sample absorption, fluorescence, and Compton scattering, the structure factors $S(Q)$ were obtained from the integrated intensities data. Pair distribution functions $G(r)$ can be obtained through Fourier transform on structure factors. Extended X-ray absorption of fine structure (EXAFS) measurements for selected samples were performed at SSRF in Shanghai. From the Fourier transformed modulating wave function $\chi(k)$ in k space, the radial distribution function of different central atoms can be obtained. Transmission electron microscope (TEM) measurements using a Philips CM20 TEM operating at 200 kV for selected samples were also applied to monitor changes in structure of studied BMGs. Electron transparent TEM lamellae were produced by mechanical grinding and polishing followed by low angle Ar-ion milling.

In order to investigate the elastic properties of the BMGs, the ultrasonic testing was taken on the disk samples that the pulse frequency used was 2.25 MHz. It can be calculated from

$$\gamma = \frac{1-2(v_t/v_l)^2}{2-2(v_t/v_l)^2}; \quad \mu = \rho v_t^2; \quad E = 2(1+\gamma)\mu; \quad B = E/3(1-2\gamma)$$

where v_l and v_t are the propagation velocities of longitudinal and transversal acoustic waves. ρ is density, γ is Poisson's ratio, μ is shear modulus, E is Young's modulus and B is bulk modulus. Densities of all studied BMGs were measured by Archimedeian principle. Room temperature compression tests were performed on cylindrical samples with a length-to-diameter aspect ratio 2:1 at an initial strain rate of 10^{-4} s^{-1} . Nanoindentation measurements with a 2.3 μm spherical indenter were performed on the polished BMG samples with a maximum load 20 mN and loading rate 0.5 mN s^{-1} . In order to observe the shear bands evolution during deformation, in-situ compression tests were also conducted in scanning electron microscope (Supra 55VP, ZEISS, Germany) with a compressor holder and a strain rate of 10^{-4} s^{-1} .

The structures of the as cast $\text{Zr}_{64-x}\text{Ni}_{10}\text{Al}_7\text{Cu}_{19}\text{Co}_x$ ($x = 0-16 \text{ at.}\%$) alloys (2 mm in diameter) were first analyzed. From XRD patterns in Fig. 1a, it is found that samples with Co content $\leq 8.3 \text{ at.}\%$ are full amorphous. Thus, in the following sections, we only focus on $\text{Zr}_{64-x}\text{Ni}_{10}\text{Al}_7\text{Cu}_{19}\text{Co}_x$ ($x = 0-8.3 \text{ at.}\%$) BMG samples. DSC results in Fig. 1b clearly reveal that the Co addition affects the thermal properties of the alloys, i.e., the single crystallization peak separates into two because the alloy composition changes from almost eutectic one to off-eutectic one. With increasing the Co content, glass transition temperature T_g of the alloy slightly moves to higher temperature while the first crystallization peaks moves to lower temperature and the second crystallization peak moves to higher temperature. All thermal parameters of the alloys are listed in Table 1.

The mechanical properties of studied BMGs were first investigated using ultrasound pulse echo technique. The obtained results are also listed in Table 1. With increasing the Co content, the Young's modulus and hardness monotonically increase, while Poisson's ratio slightly reduces first from 0.391 for the $\text{Zr}_{64}\text{Ni}_{10}\text{Al}_7\text{Cu}_{19}$ BMG to 0.385 for the $\text{Zr}_{58}\text{Ni}_{10}\text{Al}_7\text{Cu}_{19}\text{Co}_6$ BMG and then increases again to 0.393 for the $\text{Zr}_{55.7}\text{Ni}_{10}\text{Al}_7\text{Cu}_{19}\text{Co}_{8.3}$ BMG. The ratio of shear modulus to bulk modulus

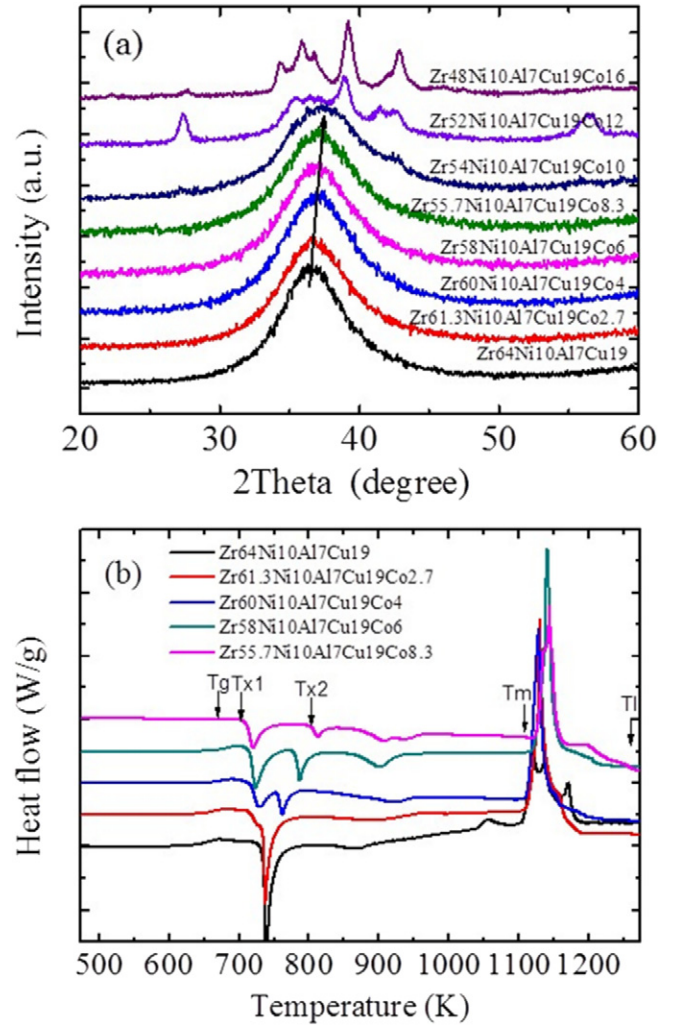


Fig. 1. (a) X-ray diffraction patterns of $\text{Zr}_{64-x}\text{Ni}_{10}\text{Al}_7\text{Cu}_{19}\text{Co}_x$ ($x = 0-16 \text{ at.}\%$) alloys and (b) DSC curves of $\text{Zr}_{64-x}\text{Ni}_{10}\text{Al}_7\text{Cu}_{19}\text{Co}_x$ ($x = 0-8.3 \text{ at.}\%$) BMGs as a function of Co content after casting in 2 mm in diameter.

increases from 0.235 to 0.250 and then decreases to 0.231. Fig. 2a displays the compressive stress-strain curves for $\text{Zr}_{64-x}\text{Ni}_{10}\text{Al}_7\text{Cu}_{19}\text{Co}_x$ ($x = 0-8.3 \text{ at.}\%$) BMGs. Concerning the plastic strain, it decreases with the addition of Co, but, for the $\text{Zr}_{55.7}\text{Ni}_{10}\text{Al}_7\text{Cu}_{19}\text{Co}_{8.3}$ BMG, it reaches about 4%, which seems to correlate with the Co content dependent Poisson's ratio and shear modulus/bulk modulus ratio [28,29]. Concerning the elastic strain limit, it seems that the elastic strain limit has an increasing tendency with the increase of Co content. If it is true, it would be interesting because the Young's modulus in Table 1 also increases with Co content. Here we should mention that the calculations of the elastic strain limit based on the stress-strain curves are relatively low accuracy due to experimental loading conditions. In order to accurately determine the elastic strain limit of all studied Zr_{64-x}

Table 1

Parameters of T_g , T_{x1} , T_{x2} , T_m , T_l , E , γ , μ/B (shear modulus/bulk modulus ratio), density and hardness as a function of Co content in $\text{Zr}_{64-x}\text{Ni}_{10}\text{Al}_7\text{Cu}_{19}\text{Co}_x$ ($x = 0-8.3 \text{ at.}\%$) BMGs.

C (Co) (at.%)	T_g (K)	T_{x1} (K)	T_{x2} (K)	T_m (K)	T_l (K)	E (GPa)	γ	μ/B	Density (g/cm ³)	Hardness (GPa)
0	648	723	–	1103	1185	74.9	0.391	0.235	6.796	5.3
2.7	654	710	730	1106	1194	78.8	0.390	0.237	6.831	5.5
4	668	710	748	1108	1203	83.6	0.388	0.241	6.846	5.9
6	670	706	769	1115	1223	81.1	0.385	0.250	6.862	5.9
8.3	675	701	794	1121	1268	84.4	0.393	0.231	6.888	6.2

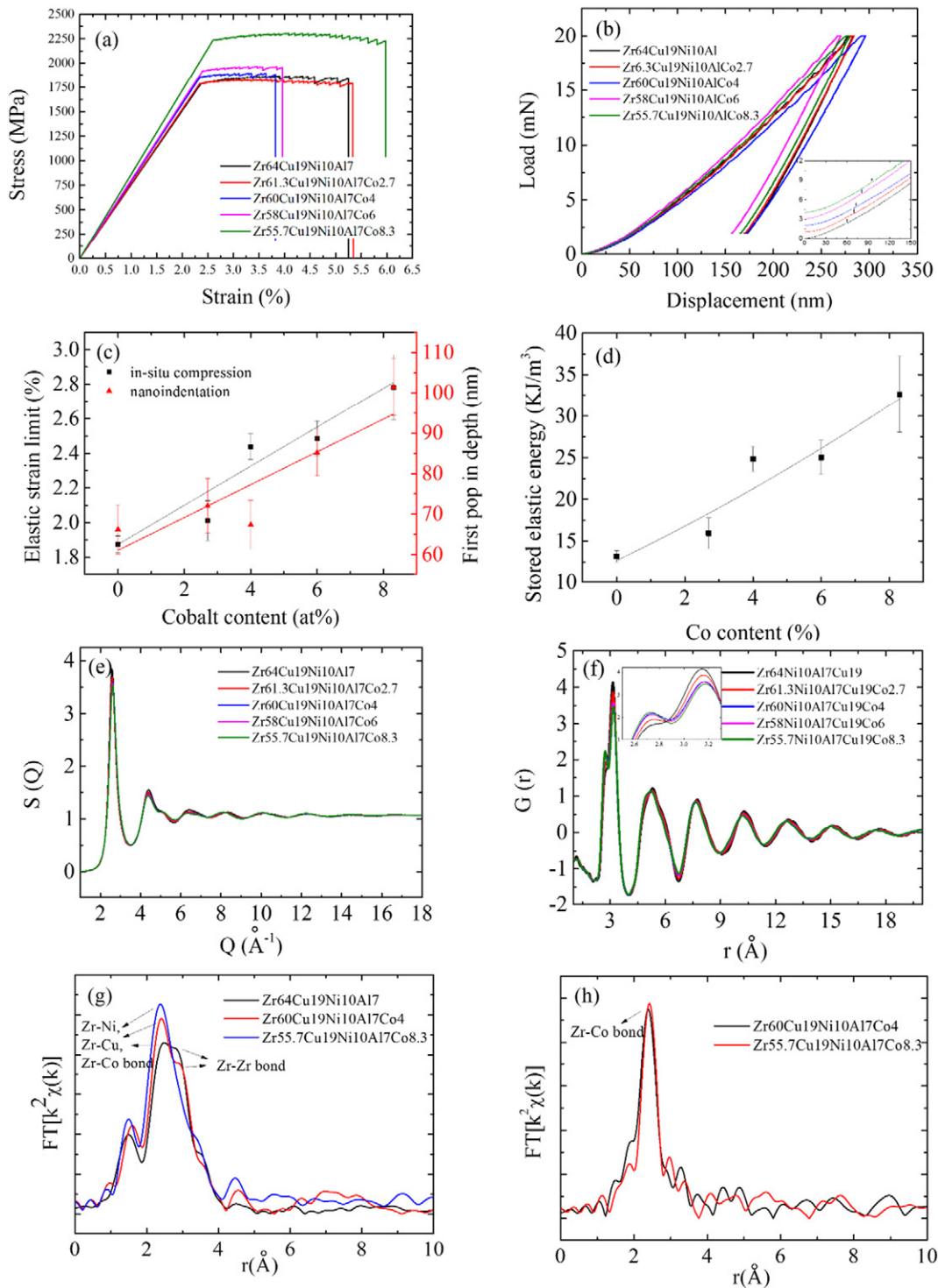


Fig. 2. (a) Compression stress-strain curves and (b) nanoindentation curves of five $\text{Zr}_{64-x}\text{Ni}_{10}\text{Al}_7\text{Cu}_{19}\text{Co}_x$ ($x = 0-8.3$ at.%) BMG samples. (c) Elastic strain limits estimated from compression measurements and yield depths at the first pop-in event estimated from panel b inset, and (d) stored elastic energies for $\text{Zr}_{64-x}\text{Ni}_{10}\text{Al}_7\text{Cu}_{19}\text{Co}_x$ ($x = 0-8.3$ at.%) BMGs as a function of Co content. (e) Structure factors, (f) pair distribution functions (and the inset is magnification of the first peaks of pair distribution functions) for $\text{Zr}_{64-x}\text{Ni}_{10}\text{Al}_7\text{Cu}_{19}\text{Co}_x$ ($x = 0-8.3$ at.%) BMG samples. Extended X-ray absorption of fine structure Zr K-edge data (g) and Co K-edge data (h) for selected $\text{Zr}_{64-x}\text{Ni}_{10}\text{Al}_7\text{Cu}_{19}\text{Co}_x$ ($x = 0-8.3$ at.%) BMG samples.

$\text{Zr}_{64-x}\text{Ni}_{10}\text{Al}_7\text{Cu}_{19}\text{Co}_x$ ($x = 0-8.3$ at.%) BMGs, nanoindentation with a spherical indenter was applied by the first pop-in event method [30], in which the elastic strain limit (i.e., it corresponds to the yield depth for the first pop-in event) can be obtained with a relatively high accuracy in Fig. 2b. The yield depth in Fig. 2c, which are averaged by ten indentation tests, indeed increases with Co content, which is consistent with the results obtained by compression tests in Fig. 2a.

The diatomic gas model, which was proposed by Guinier [31], and applied by various groups [32–35], can roughly monitor the change of the average interatomic distance in bulk metallic glasses. The average interatomic distance in BMGs to the Bragg diffraction equation is expressed by: $K\lambda = 2d\sin\theta_m$, where θ_m is the maximal diffracted intensity angle, λ is the radiation wavelength, d is the atomic distance of a diatomic gas, K is constant. For the diatomic gas model, K is 1.23. In Fig. 1a,

it is observed that the diffraction peak position of the first maximum in BMG samples increases with the Co content. This means that the higher the Co content in the $Zr_{64-x}Ni_{10}Al_7Cu_{19}Co_x$ ($x = 0-8.3$ at.%) BMGs, the shorter the average atomic distance. Structure factor and pair distribution function are further applied to deepen our understanding to the atomic structure changes in the studied $Zr_{64-x}Ni_{10}Al_7Cu_{19}Co_x$ ($x = 0-8.3$ at.%) BMGs. All studied BMG samples have similar structure factors in Fig. 2e and pair distribution functions in Fig. 2f. With careful examination of the first peak in $G(r)$ in the inset of Fig. 2f, it is found that with increasing the Co content the amplitude of the peak ($r \approx 3.12$ Å) in PDFs is reduced while the left-side shoulder ($r \approx 2.72$ Å) increases. These results indicate that with increasing the Co content, the reduction of the average atomic distance is resulted from the rearrangement of atomic packing by forming a new topological structure with shorter atomic bonds, consistent with the increase of densities in Table 1. In order to confirm the atomic bonds changes, Co— and Zr—K edge EXAFS measurements for some selected BMG samples are carried out in Fig. 2h and g. No obvious change on Co K-edge EXAFS in Fig. 2h was detected in both $Zr_{60}Ni_{10}Al_7Cu_{19}Co_4$ and $Zr_{55.7}Ni_{10}Al_7Cu_{19}Co_{8.3}$ BMGs, which could be reflected from the fact that the average atomic surrounding around Co atoms is not affected by low Co content. The intensity of Zr—Zr bonds peak in Fig. 2g reduces while the intensities of Zr—Ni, Zr—Cu, or/and Zr—Co bonds peaks (which have similar bond lengths and are not distinguished from each other) increase with increasing the Co content. At the same time, the maximum points of Zr—Ni, Zr—Cu, or/and Zr—Co bonds peaks shift to left which means a smaller average atomic bonds length. It can be concluded that the new topological structure is formed by Zr—Co bonds, which are shorter and stronger than Zr—Zr and Zr—Cu bonds, leading to the reduction of the average atomic distance in studied $Zr_{64-x}Ni_{10}Al_7Cu_{19}Co_x$ ($x = 0-8.3$ at.%) BMGs. We believe that these stronger Zr—Co bonds formed in Co-containing BMGs contribute to the enhancement of elastic strain limit, T_g , hardness and Young's modulus [36]. The morphology evolution of studied $Zr_{64-x}Ni_{10}Al_7Cu_{19}Co_x$ ($x = 0-8.3$ at.%) BMGs was carried out by backscattering SEM measurements. Only homogeneous structure on micrometer scale for all studied BMGs was detected. We further performed electron diffraction and high resolution TEM investigations for two $Zr_{64}Ni_{10}Al_7Cu_{19}$ and $Zr_{55.7}Ni_{10}Al_7Cu_{19}Co_{8.3}$ BMG samples in Fig. 3. Electron diffraction patterns show amorphous composition for both samples. But HRTEM images revealed a nanometer scaled inhomogeneous on $Zr_{55.7}Ni_{10}Al_7Cu_{19}Co_{8.3}$ BMG sample, as compared to the $Zr_{64}Ni_{10}Al_7Cu_{19}$ BMG. It seems that phase separation in a scale of 5–10 nm regions should occur in the $Zr_{55.7}Ni_{10}Al_7Cu_{19}Co_{8.3}$ BMG sample. It could be caused by the positive mixing enthalpy between copper and cobalt which can also be proved by left shifting of peaks on EXAFS results (Fig. 2g) that not only Zr—Zr bonds but also Zr—Cu bonds are replaced by Zr—Co bonds. Unfortunately, locally performed EDX point analysis with 10 nm spatial resolution could not detect phase separation which were smaller than 5 nm. High resolution EDX mapping using scanning TEM and atom probe tomography are planned for future investigation.

As discussed earlier, Co content does affect the plastic behavior, Poisson's ratio and the ratio of shear modulus to bulk modulus of $Zr_{64-x}Ni_{10}Al_7Cu_{19}Co_x$ ($x = 0-8.3$ at.%) BMGs in Fig. 2 and Table 1. We further performed in-situ compression experiments in SEM for three selected BMGs, during which micrographs and videos were taken to monitor the evolution of shear bands. Fig. 4 shows images for three BMG samples with different Co contents at their yield points. Many shear bands are detected on the surface of both $Zr_{64}Ni_{10}Al_7Cu_{19}$ and $Zr_{55.7}Ni_{10}Al_7Cu_{19}Co_{8.3}$ BMG samples, while for the $Zr_{58}Ni_{10}Al_7Cu_{19}Co_6$ BMG sample, only a few shear bands can be observed. These observations are consistent with the results observed in Fig. 2, i.e., the more shear bands, the larger the plastic strain. The formation of denser topological structure (i.e., the enhancement of the shoulder in the first peak of PDFs and of stronger Zr—Co bonds in EXAFS) could reduce the amount of shear transformation zones (STZ) in the $Zr_{58}Ni_{10}Al_7Cu_{19}Co_6$ BMG sample

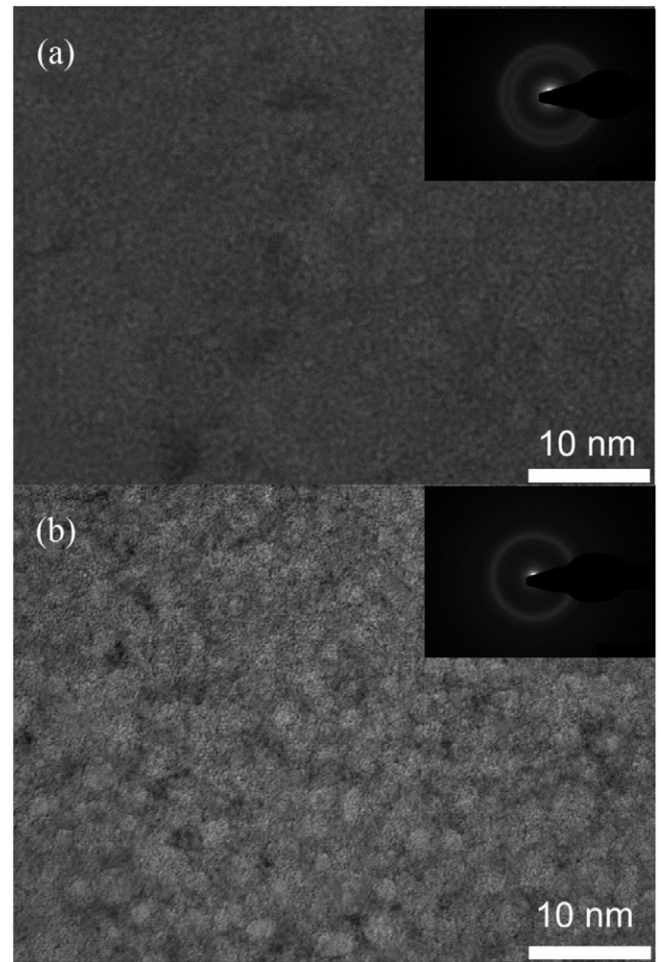


Fig. 3. Transmission electron microscope images of two BMG samples (a) $Zr_{64}Ni_{10}Al_7Cu_{19}$ and (b) $Zr_{55.7}Ni_{10}Al_7Cu_{19}Co_{8.3}$.

[37–40]. On the other hand, for the $Zr_{55.7}Ni_{10}Al_7Cu_{19}Co_{8.3}$ BMG sample, phase separation phenomenon becomes obviously and sufficient second phase and interfaces exist in the BMG sample. Consequently, the propagation directions of shear bands during compression could be altered [41–43], as supported by the observation of the intersection of shear bands with different orientations, resulting in the improvement of ductility of this BMG sample. Furthermore, the Co content dependent elastic strain limit in $Zr_{64-x}Ni_{10}Al_7Cu_{19}Co_x$ ($x = 0-8.3$ at.%) BMGs detected in Fig. 2c, was also confirmed by the sample length measurements at zero stress and at yielding point during in situ SEM compression. Both compression tests and nanoindentation measurements coincidentally reveal that the $Zr_{55.7}Ni_{10}Al_7Cu_{19}Co_{8.3}$ BMG sample has high elastic strain limit (about 2.8%), which is higher than many reported values for other BMGs (1.8–2%). The reason for the high elastic strain limit could be linked with the fact that the second phase and/or interfaces between two glassy phases hinder the shear bands propagation, resulting in higher critical shear stresses for activating shear bands [44–45].

Consequently, the stored recoverable elastic energy ($\sim E\epsilon^2$), as shown in Fig. 2d, increases also with Co content. With these good properties, i.e., about 2.8% elastic strain limit, about 2.3 GPa yielding strength, about 4% compression plastic strain, Young modulus of 84.4 GPa, Poisson ratio of 0.393 and shear modulus/bulk modulus ratio of 0.231, the $Zr_{55.7}Ni_{10}Al_7Cu_{19}Co_{8.3}$ BMG might be a good material for micromechanics and sports equipment applications. This work reveals that minor alloying, having positive enthalpy of mixing with other components, is a good method to improve mechanical properties of BMGs

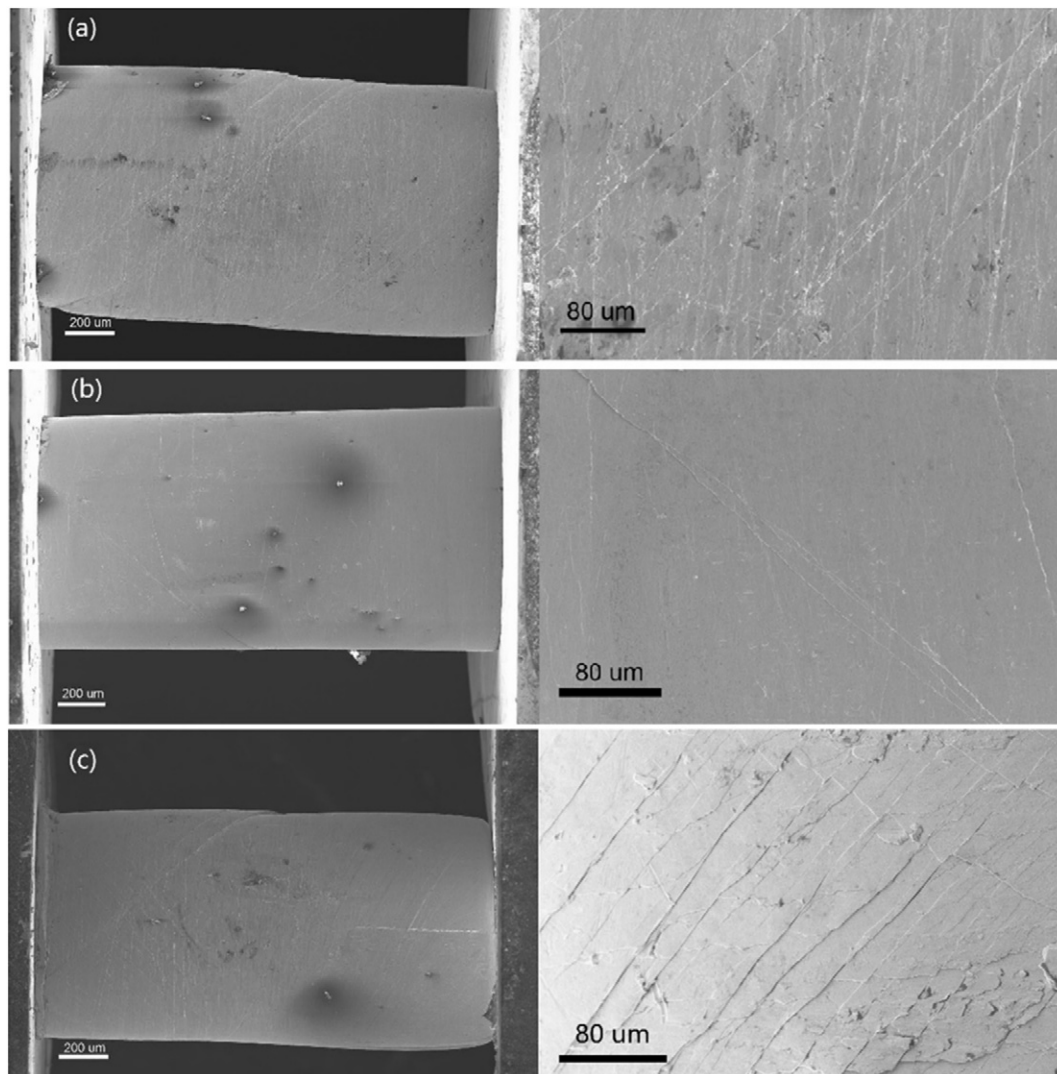


Fig. 4. In-situ compression SEM images at yield points for three BMG samples (a) $\text{Zr}_{64}\text{Ni}_{10}\text{Al}_7\text{Cu}_{19}$, (b) $\text{Zr}_{58}\text{Ni}_{10}\text{Al}_7\text{Cu}_{19}\text{Co}_6$, and (c) $\text{Zr}_{55.7}\text{Ni}_{10}\text{Al}_7\text{Cu}_{19}\text{Co}_{8.3}$.

via the formation of heterogeneous structures. However, sometimes, the glass forming ability is reduced after minor alloying. Different elements could have different effects on solidification. The formed intermetallic compounds are brittle which have negative effects on mechanical performance. In order to obtain good properties of BMGs, the size distribution of newly-formed phase(s) should be considered.

Acknowledgments

Financial supports from the National Key Research and Development Program of China (No. 2016YFB0701203 and 2016YFB0700201), the National Natural Science Foundation of China (51371157, U1432105, U1432110, U1532115, 51671170 and 51671169), the Natural Science Foundation of Zhejiang Province (grants Z1110196 and Y4110192), the DAAD cooperation and the Fundamental Research Funds for the Central Universities are gratefully acknowledged.

Appendix A. Supplementary data

Supplementary Video 1 In-situ compression (Co0)
 Supplementary Video 2 In-situ compression (Co6)
 Supplementary Video 3 In-situ compression (Co8.3)

References

- [1] A. Inoue, *Acta Mater.* 48 (2000) 279.
- [2] A.L. Greer, Y.Q. Cheng, E. Ma, *Mater. Sci. Eng. R* 74 (2013) 71–132.
- [3] A. Peker, W.L. Johnson, *Appl. Phys. Lett.* 63 (1993) 2342.
- [4] W.H. Wang, C. Dong, C.H. Shek, *Mater. Sci. Eng. R* 44 (2004) 45.
- [5] F. Szeucs, P.C. Kim, W.L. Johnson, *Acta Mater.* 49 (2001) 1513–1570.
- [6] M.M. Trexler, N.N. Thadhani, *Prog. Mater. Sci.* 55 (2010) 759–839.
- [7] O.V. Kuzmin, Y.T. Pei, C.Q. Chen, J.T.M. De Hosson, *Acta Mater.* 60 (2012) 889–898.
- [8] E.S. Park, J.H. Na, D.H. Kim, *Appl. Phys. Lett.* 91 (2007), 031907.
- [9] R. Wunderlich, M.L. Vaillant, A. Caron, H.-J. Fecht, *Adv. Eng. Mater.* 10 (2008) 1020–1025.
- [10] C.N. Kuo, J.C. Huang, X.H. Du, X.J. Liu, T.G. Nieh, *J. Alloys Compd.* 586 (2014) S14–S19.
- [11] D.C. Hofmann, J.-Y. Suh, A. Wiest, G. Duan, M.-L. Lind, M.D. Demetr, W.L. Johnson, *Nature* 451 (2008) 1085–1089.
- [12] Y. Wu, Y.H. Xiao, G.L. Chen, C.T. Liu, Z.P. Lu, *Adv. Mater.* 22 (2010) 2770–2773.
- [13] Z.Q. Liu, R. Li, G. Liu, W.H. Su, H. Wang, Y. Li, M.J. Shi, X.K. Luo, G.J. Wu, T. Zhang, *Acta Mater.* 60 (2012) 3128–3139.
- [14] H. Gleiter, *Acta Mater.* 56 (2008) 5875–5893.
- [15] X.D. Wang, Q.P. Cao, J.Z. Jiang, H. Franz, J. Schroers, R.Z. Valiev, Y. Ivanisenko, H. Gleiter, H.-J. Fecht, *Scr. Mater.* 64 (2011) 81.
- [16] X.L. Wang, F. Jiang, H. Hahn, J. Li, H. Gleiter, J. Sun, J.X. Fang, *Scr. Mater.* 116 (2016) 95–99.
- [17] Y. Ritter, D. Sopu, H. Gleiter, K. Albe, *Acta Mater.* 59 (2011) 6588–6593.
- [18] X.H. Du, J.C. Huang, K.C. Hsieh, Y.H. Lai, H.M. Chen, J.S.C. Jang, P.K. Liaw, *Appl. Phys. Lett.* 91 (2007) 131901.
- [19] L.Y. Chen, Z.D. Fu, G.Q. Zhang, X.P. Hao, Q.K. Jiang, X.D. Wang, Q.P. Cao, H. Franz, Y.G. Liu, H.S. Xie, S.L. Zhang, B.Y. Wang, Y.W. Zeng, J.Z. Jiang, *Phys. Rev. Lett.* 100 (2008), 075501.
- [20] X.H. Du, J.C. Huang, K.C. Hsieh, J.S.C. Jang, P.K. Liaw, H.M. Chen, H.S. Chou, Y.H. Lai, *Adv. Eng. Mater.* 11 (2009) 5.

- [21] A. Inoue, T. Zhang, T. Masumoto, *Mater. Trans.* 31 (1990) 177–183.
- [22] Y.H. Liu, G. Wang, R.J. Wang, D.Q. Zhao, M.X. Pan, W.H. Wang, *Science* 315 (2007) 1385–1388.
- [23] Q.P. Cao, J.W. Liu, K.J. Yang, F. Xu, A. Minkow, H.-J. Fecht, J. Ivanisenko, L.Y. Chen, X.D. Wang, S.X. Qu, J.Z. Jiang, *Acta Mater.* 58 (2010) 1276.
- [24] J.W. Liu, Q.P. Cao, L.Y. Chen, X.D. Wang, J.Z. Jiang, *Acta Mater.* 58 (2010) 4827.
- [25] X.P. Nie, X.H. Yang, Y. Ma, L.Y. Chen, K.B. Yeap, K.Y. Zeng, D. Li, J.S. Pan, X.D. Wang, Q.P. Cao, S.Q. Ding, J.Z. Jiang, *Corros. Sci.* 53 (2011) 3557.
- [26] T. Takeuchi, A. Inoue, *Mater. Trans.* 41 (2000) 1372–1378.
- [27] T. Takeuchi, A. Inoue, *Mater. Trans.* 12 (2005) 2817–2829.
- [28] J. Schroers, W.L. Johnson, *Phys. Rev. Lett.* 93 (2004) 255506.
- [29] P. Yu, H.Y. Bai, *Mater. Sci. Eng. A* 485 (2008) 1–4.
- [30] H. Bei, Z.P. Lu, E.P. George, *Phys. Rev. Lett.* 93 (2004) 125504.
- [31] A. Guinier, *X-ray Diffraction in Crystals, Imperfect Crystals and Amorphous Bodies*, Dover, New York, 1994.
- [32] T.C. Hufnagel, S. Brennan, *Phys. Rev. B* 67 (2003), 014203.
- [33] J.Z. Jiang, J.S. Olsen, L. Gerward, S. Abdali, J. Eckert, N. Schlorke, L. Schultz, J. Truelsenbrodt, P.X. Shi, *J. Appl. Phys.* 87 (2000) 2664.
- [34] J.Z. Jiang, W. Roseker, M. Sikorski, Q.P. Cao, F. Xu, *Appl. Phys. Lett.* 84 (2004) 1871.
- [35] Q.K. Jiang, Z.Y. Chang, X.D. Wang, J.Z. Jiang, *Metall. Mater. Trans. A* 41 (2010) 1634.
- [36] A. Concustell, J. Sort, A.L. Greer, *Appl. Phys. Lett.* 88 (2006) 171911.
- [37] P. Donovan, *Acta Mater.* 37 (1989) 445–456.
- [38] F. Yuan, V. Prakash, Lewandowski, *SEM IX International Congress on Experimental and Applied Mechanics* 336 (2008).
- [39] F. Yuan, V. Prakash, Lewandowski, *J. Mater. Res.* 22 (2007) 402–411.
- [40] M. Martin, L. Kecskes, N. Thadhani, *Scr. Mater.* 59 (2008) 688–691.
- [41] M.A. Meyer, *J. Physiol. Paris* 4 (1994) C8–597.
- [42] C.C. Hays, C.P. Kim, W.L. Johnson, *Phys. Rev. Lett.* 84 (2000) 2901.
- [43] Q. Zheng, H. Ma, E. Xu, J. Ma, *Scr. Mater.* 55 (2006) 541.
- [44] B.P. Kanungo, S.C. Glade, P.A. Kumar, K.M. Flores, *Intermetallics* 12 (2004) 1073.
- [45] T. Ichitsubo, *Phys. Rev. Lett.* 95 (2005) 245501.